Catalogue of the morphological features in the Spitzer Survey of Stellar Structure in Galaxies (S^{4}G) ⋆

M. Herrera-Endoqui[1], S. Díaz-García[1], E. Laurikainen[1, 2], and H. Salo[1]

[1] Astronomy and Space Physics, University of Oulu, FI-90014, Finland
  e-mail: martin.herreraendoqui@oulu.fi
[2] Finnish Centre of Astronomy with ESO (FINCA), University of Turku, Väisäläntie 20, FI-21500, Piikkiö, Finland

ABSTRACT

Context. A catalogue of the features for the complete Spitzer Survey of Stellar Structure in Galaxies (S^{4}G), including 2352 nearby galaxies, is presented. The measurements are made using 3.6 μm images, largely tracing the old stellar population; at this wavelength the effects of dust are also minimal. The measured features are the sizes, ellipticities, and orientations of bars, rings, ringlenses, and lenses. Measured in a similar manner are also barlenses (lens-like structures embedded in the bars), which are not lenses in the usual sense, being rather the more face-on counterparts of the boxy/peanut structures in the edge-on view. In addition, pitch angles of spiral arm segments are measured for those galaxies where they can be reliably traced. More than one pitch angle may appear for a single galaxy. All measurements are made in a human-supervised manner so that attention is paid to each galaxy.
Aims. We create a catalogue of morphological features in the complete S^{4}G.
Methods. We used isophotal analysis, unsharp masking, and fitting ellipses to measured structures.
Results. We find that the sizes of the inner rings and lenses normalized to barlength correlate with the galaxy mass: the normalized sizes increase toward the less massive galaxies; it has been suggested that this is related to the larger dark matter content in the bar region in these systems. Bars in the low mass galaxies are also less concentrated, likely to be connected to the mass cut-off in the appearance of the nuclear rings and lenses. We also show observational evidence that barlenses indeed form part of the bar, and that a large fraction of the inner lenses in the non-barred galaxies could be former barlenses in which the thin outer bar component has dissolved.

Key words. Astronomical databases: Atlases – Astronomical databases: Catalogues – Galaxies: statistics – Galaxies: structure

1. Introduction

Galactic disks formed at redshifts z ∼ 1 - 2.5 when the Universe was still clumpy and contained a large amount of gas (White & Rees 1978; Bournaud et al. 2007; Dekel et al. 2009), in which era galaxy encounters were also frequent. The disks formed at high redshifts were smaller and less massive than in the local universe, which means that a significant amount of mass was later accreted to galaxies, and that accretion still continues at some level. When most of the mass accretion had terminated, galaxies started to evolve more slowly, by star formation and by internal dynamical effects, rearranging the mass distribution in galaxies (Kormendy & Kennicutt 2004). As imprints of this evolution, galactic disks have such morphological structures as bars, rings, lenses, and spiral arms. By studying these features at mid-infrared (mid-IR) wavelengths we obtain information about the long-term secular evolution in galaxies.

Bars can already form at z=2 (Simmons et al. 2014), but those bars are not as frequent, and not yet similar to the bars in the nearby universe, where even two-thirds (Eskridge et al. 2000; Buta et al. 2015) of the galaxies have bars. At 3.6 μm bars appear in 55% of the S0/a-Sc galaxies, and even in 81% of Hubble stages Scd-Sm (Buta et al. 2015). In these very late-type galaxies bars are more knotty, and typically the galaxies are

not centrally concentrated. Bars also evolve, for example from buckling instabilities (Combes & Sanders 1981; Pfenniger & Friedli 1991), which lead to vertically thick boxy/peanut shape bulges frequently observed in the edge-on view (Jarvis 1986; Lütticke et al. 2000; Bureau et al. 2006; Yoshino & Yamauchi 2015). In the more face-on view boxy/peanut structures appear as barlenses embedded in bars (Laurikainen et al. 2011, 2014; Athanassoula et al. 2014). By appearance alone, barlenses are easily misinterpreted as classical bulges.

Rings appear at the resonances of bars (see Schwarz 1981; Buta & Combes 1996), although other explanations for the formation of rings have also been suggested (see Athanassoula et al. 2010). There are nuclear, inner, and outer rings, as well as their different varieties. In a similar manner there are also nuclear, inner, and outer lenses (Kormendy 1979; Laurikainen et al. 2011). The sizes, shapes, and orientations of these structures tie them into the internal dynamical evolution of galaxies (see Buta & Combes 1996). These structures are further connected both to visible and dark matter content in galaxies. However, rings and lenses are not limited to barred galaxies (Grouchy et al. 2010; Laurikainen et al. 2013), and particularly for lenses explanations other than the resonant origin are generally given. For example, minor mergers can create lenses similar to those observed in the non-barred early-type galaxies (Eliche-Moral et al. 2012). Lenses are also suggested to form from disk instabilities (Athanassoula 1983), truncated star formation (Bosma 1983), or they might have formed via dissolution of bars into lenses (Ko-

---

rmendy 1979). It has also been suggested, based on their similarity in size, that inner lenses in the non-barred galaxies might be former barlenses in which the outer thin bar component has dissolved (Laurikainen et al. 2013).

Spiral arms are generally considered as density waves propagating in the stellar disk. Morphology of the spiral arms is connected to the physical properties of the galaxies. For example, pitch angle is found to correlate with the central mass concentration and the density of the HI gas in galaxies (Davis et al. 2015). It also depends on the total galaxy mass so that the spiral arms are more open in galaxies with rising rotation curves, whereas those with falling rotation curves are generally tightly wound (Seigar et al. 2005, 2006, 2014). The arms are more flocculent in the low mass galaxies (Elmegreen & Elmegreen 1985; Elmegreen et al. 2011), where the dark matter halos are also likely to be more dominant. Spiral arms can also be triggered by bars or by tidal interactions (see Kormendy & Norman 1979; Seigar et al. 2003; Salo et al. 2010). In fact, the most prominent grand-design spiral arms appear in interacting galaxies like M51. Spiral arms can also participate in the formation of inner disks or disk-like pseudobulges, both in barred and non-barred galaxies (Carollo et al. 2002; Boeker et al. 2004; Emsellem et al. 2015). Spiral arms are generally delineated by strong star forming regions observed in the UV and optical, but the mid-IR wavelength used in this study allows a more reliable characterization of the spiral arms as a density response to the long-term dynamical effects in galaxies.

In the current study we present a catalogue of the structure components in the Spitzer Survey of Stellar Structure in Galaxies (S^{4}G; Sheth et al. 2010), which contains over 2000 nearby galaxies observed at mid-IR wavelengths. We use the 3.6 μm images to measure the sizes, orientations, and ellipticities of bars, rings, and lenses. In a similar manner we also measure barlenses, which actually form part of the bar. For the spiral galaxies the pitch angles of the spirals arms are also measured. We use these measurements to discuss the nature of rings, lenses, and barlenses in the complete S^{4}G.

2. Sample and the database

We use the Spitzer Survey of Stellar Structure in Galaxies (S^{4}G; Sheth et al. 2010), which is a survey of 2352 galaxies observed at 3.6 and 4.5 μm with the Infrared Array Camera (IRAC; Fazio et al. 2004) on board the Spitzer Space Telescope. This survey is limited in volume (d<40 Mpc, |b| > 30 deg), magnitude, corrected for internal extinction (B$_{corr}$ < 15.5), and size (D$_{25}$ > 1 arcmin). It covers all Hubble types and disk inclinations. However, as the sample was originally selected based on the HI 21 cm radial velocities (V$_{radio}$ < 3000 km/sec) it lacks gas-poor early-type galaxies. To correct this bias, a supplementary sample of 465 early-type galaxies that fulfil the same selection criteria (Sheth et al. 2013) will be included in the sample and studied in a future work. The S^{4}G extends to lower galaxy luminosities than most previous samples of barred galaxies.

The 3.6 μm images used in this study allow a dust-free view (Draine & Lee 1984) of the old stellar population in galaxies. However, although the 3.6 μm largely traces the mass in galaxies, this wavelength is also contaminated by emission from hot dust, and by 3.3 μm emission features from polycyclic aromatic hydrocarbon (PAH) associated with star forming regions (see Meidt et al. 2012). Although this is a drawback while estimating the mass distribution of galaxies, it has the advantage that in the same images we can see the star forming regions even in the locations that are obscured by dust in the optical region. The

S^{4}G images are deep, typically reaching azimuthally averaged stellar mass surface densities of 1M$_\odot$ pc^{-2}. The spiral arms can be followed up to 1.5 R$_{25}$ (R$_{25}$ is the radius at the optical B-band surface brightness of 25 mag arcsec^{-2}), which is more than in most previous optical and near-IR studies. The pixel scale at 3.6 μm is 0.75" and the resolution in terms of FWHM is 2.1" (Salo et al. 2015, ApJS, in press). With this resolution not all possible nuclear bars, nuclear rings, or nuclear lenses are visible.

The S^{4}G images are processed through pipelines, including mosaic making of the raw data (P1), making of masks of the foreground stars (P2) and image defects, deriving the basic photometric parameters (P3, Muñoz-Mateos et al. 2015), and making multi-component decompositions to the 2D flux distributions of the galaxies (P4, Salo et al. 2015). We use the mosaicked 3.6 μm band images from Muñoz-Mateos et al. The estimations of the sky background levels and the orientation parameters of the disks are from Salo et al.

3. Measured structure components

In this study the identification of the structure components is based on the mean de Vaucouleurs revised Hubble-Sandage morphological classification made by Buta et al. (2015) at 3.6 μm. Concerning the details in morphology, this is the most complete classification done so far in the spirit of de Vaucouleurs and Sandage. It includes the stage (E, E+, S^0, S0^0, S0$^+$, S0/a, Sa, Sab, Sb, Sbc, Sc, Scd, Sd, Sdm, Sm, Im), family (SA, SAB, SB), and variety (r, rs, s), as well as nuclear, inner and outer rings, ringlenses, and lenses. It also includes other fine-structures like barlenses, X-shaped bar morphologies, and ansae (or handles) seen at the two ends of the bar. Notations of the different structure components that are considered in this study are shown in Table 1. In uncertain cases the underscore in the classification shows what is the most likely identification of the structure. The exact meaning of the notations can be found in the original classification paper by Buta et al. (2015). Altogether the number of features identified in the classification by Buta et al., and those that we measured are: 1174/1146 bars, 805/799 rings, 294/294 lenses and ringlenses, 90/87 nuclear structures, and 67/67 barlenses, respectively.

From the point of view of our measurements the structure components are defined in the following manner:

Rings (R, r, nr)

Resonance rings are features that have well-defined inner and outer edges. The rings can be full or non-complete pseudorings, which are further divided into different subtypes (Buta et al. 2015). Rings are located at the resonances of bars. Outer rings are generally associated with outer Lindblad resonance (OLR) and typically have sizes roughly twice the size of the bar (Athanassoula et al. 1982), depending also on the rotation curve. The OLR subtypes are R$_1$, R$_1$', R$_2$', and R$_1$R$_2$'. Inner rings are associated with the inner 1/4 ultraharmonic resonance (UHR) and have sizes similar to those of bars. Nuclear rings are located at the inner Lindblad resonance (ILR) of the bar, and typically have sizes of hundreds of parsecs (Buta 1986). In the non-barred galaxies the notation of nuclear, inner, and outer features is based on their relative size with respect to the size of the underlying disk. In this study we do not study polar rings or collisional rings formed in galaxy interactions.

Table 1. Notation of ring and lens structures.

Notation	Structure
R	Outer ring
R'	Outer pseudo-ring
R₁	Outer ring with type 1 morphology
R'₁	Outer pseudo-ring with type 1 morphology
R₂	Outer ring with type 2 morphology
R'₂	Outer pseudo-ring with type 2 morphology
_R_L, RL, R_L_	Outer ringlens
_R_'L, R'L, R'_L_	Outer pseudo-ringlens
L	Outer lens
r	Inner ring
r', _r_s, rs, r_s_	Inner pseudo-ring
_r_l, rl, r_l_	Inner ringlens
_r_'l, r'l, r'_l_	Inner pseudo-ringlens
l, ls, sl	Inner lens
bl	Barlens
nr	Nuclear ring
nr'	Nuclear pseudo-ringlens
nrl	Nuclear ringlens
nr'l	Nuclear pseudo-ringlens
nl	Nuclear lens
nl'	Nuclear lens (not fully developed)
Combinations:	
R'₁R'₂	Outer pseudo-ring with type 1 and 2 morphology
R₁L	Outer ringlens with type 1 morphology
R₁'L	Outer pseudo-ringlens with type 1 morphology
R₂L	Outer ringlens with type 2 morphology
R₂'L	Outer pseudo-ringlens with type 2 morphology

Lenses(L, l, nl)

Just as there are nuclear, inner, and outer rings, there are also nuclear, inner, and outer lenses. Kormendy (1979) defined lenses as structures with shallow brightness gradient interior to a sharp outer edge, and a steep gradient thereafter. They form part of the original classification by Sandage (1961) and Sandage & Bedke (1994), but have been systematically coded into the classification only recently by Laurikainen et al. (2011) and Buta et al. (2015). Like the inner rings, the inner lenses in barred galaxies have similar sizes to the bar, whereas the outer lenses are, by definition, much larger than bars.

Ringlenses (RL, rl, nrl)

Ringlenses are also divided into nuclear, inner, and outer structures. They are intermediate types between rings and lenses. Ringlenses resemble rings in that they have outer edges, and lenses in that the inner radius is smoother than in the rings.

Barlenses (bl)

Barlenses were recognized as distinct features by Laurikainen et al. (2011). They were defined as lens-like structures embedded in bars, typically having sizes of ∼ 50% of the bar size, which means that they are considerably larger than the nuclear lenses. In appearance barlenses resemble prominent bulges, but are different from them in that their surface brightness profiles drop faster at the edges. The surface brightness profiles along the minor and major axes of a barlens are fairly exponential (Laurikainen et al. 2014). Barlenses are not lenses in the same way as the other type of lenses, being rather the face-on counterparts of the vertically thick boxy/peanut structures of bars (Laurikainen

et al. 2014; Athanassoula et al. 2014; see also review by Laurikainen & Salo 2015).

Spiral arms

There are three main types of spiral arms: grand design, flocculent, and multi-arm (Elmegreen & Elmegreen 1989). Grand design galaxies have a well-defined two-armed spiral pattern, while flocculent galaxies have multiple spiral arm segments. The opening of the spiral arm is defined by the pitch angle, defined as the angle between the tangent to the spiral arm, and the tangent to a circle in a point at some radius from the galaxy centre. The pitch angle is not necessarily constant within a galaxy. It can stay nearly constant in certain regions of the galaxies (Davis et al. 2012), or can change smoothly along the galaxy radius even in grand design galaxies (Davis et al. 2015). Possible reasons for these changes are discussed by Davis et al. (2015). Furthermore, the spiral arms often appear asymmetrically at the two sides of the galaxies (see Elmegreen et al. 2011).

In the current study we identify and fit the different arm segments. Our approach takes both the radial variations and possible asymmetric nature of the spiral arms into account. A detailed morphological spiral arm classification is described by Elmegreen & Elmegreen (1989) and Elmegreen et al. (2011).

4. Preparation of the catalogue

In the catalogue we present the measurements of the dimensions of the structure components identified in the classification by Buta et al. (2015). The measured properties are the sizes, axial ratios, and orientations of the structure components. For bars the lengths are estimated both visually and from the isophotal ellipticity profiles. For spiral galaxies the pitch angles of the measured spiral arm segments are also given. All measurements are made with an interactive process in which the features are first marked on top of the images, and after that ellipses or lines are fitted to the marked points.

Typical examples of the measured structure components are shown in Figure 1, where examples of rings, ringlenses, and lenses are given. On top of the images the size measurements of the different components are drawn. For the sake of clarity not all measured structures are drawn for these example galaxies. Figure 2 illustrates the difference in size between the nuclear ring and the barlens in NGC 4314. Originally, this image appeared in Laurikainen et al. (2011). Such a large difference in size between barlenses and nuclear features is typical for all galaxies with these structures.

The catalogue consists of tables (Table 2 for bars, rings, lenses, ringlenses and barlenses, and Table 3 for spiral parameters) of the measurements for all the structure components, and of a web page where a page similar to Figure 3 appears for each galaxy[1] In Figure 3 the two upper panels show the original 3.6 μm image: in the right panel the sizes of the measured features are marked on top of the image. The middle panel shows an unsharp mask image and gives the main measured parameters. The a_{sky} is the semi-major axis length, ϵ_{sky} is the ellipticity of the structure, and PA_{sky} is the position angle. A quality flag indicates our estimation of the reliability of the fit: 1 indicates a good fit for a feature which is unambiguously identified, 2 indicates a hard-to-trace feature (due to low contrast with the rest of the galaxy), and 3 indicates an uncertain feature (due to high inclination of the host galaxy or an incomplete feature).

---

[1] http://www.oulu.fi/astronomy/S4G_STRUCTURES/main.html

NGC 1350   (R)SAB$_a$(r,bl)0/a

NGC 1533   (RL)SB(bl)0^0

NGC 1291   (R)SAB(l,bl,nb)0$^+$

NGC 2655   (L)SAB(s)0/a, pec
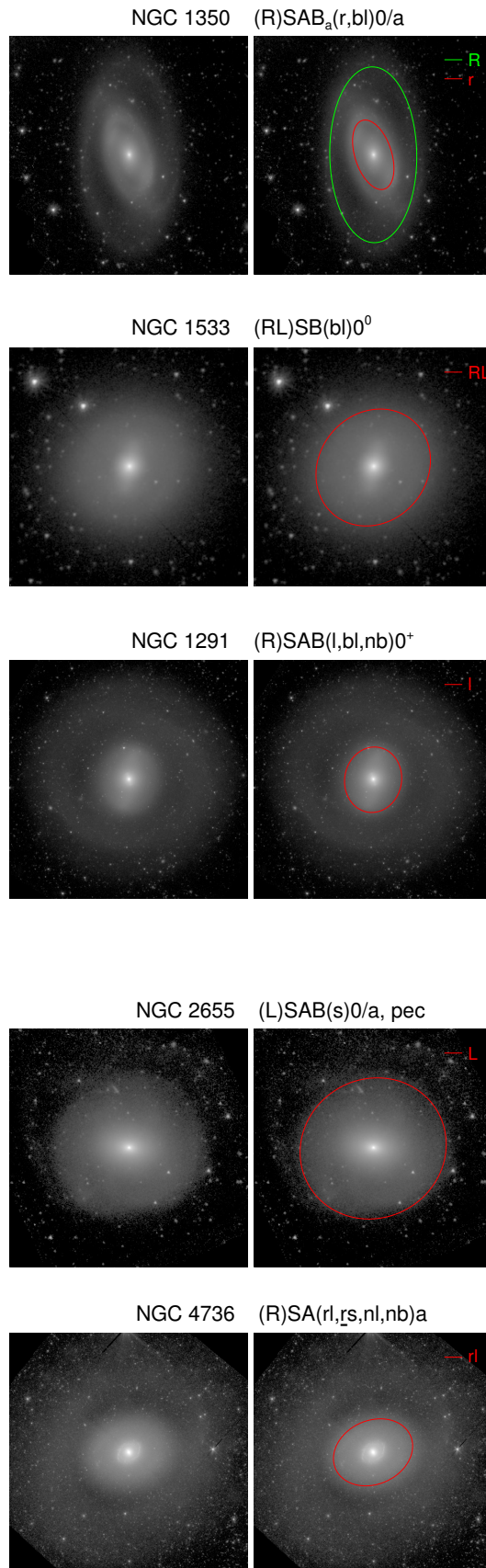
NGC 4736   (R)SA(rl,r̲s,nl,nb)a

Fig. 1. Examples of the structure components identified in the classification by Buta et al. (2015). In each case one or more of the measured features are shown on top of the 3.6 μm images from S^{4}G.

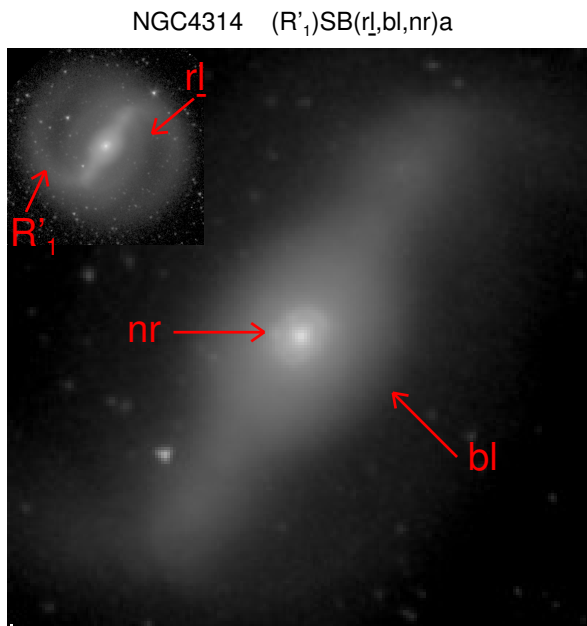NGC4314   (R'$_1$)SB(r$\underline{l}$,b$\underline{l}$,n$\underline{r}$)a

Fig. 2. NGC 4314 is a typical example of a galaxy having a barlens embedded inside the bar. The image of the bar region illustrates the size difference between the nuclear features, compared to the size of a barlens. Both the star forming nuclear ring and the barlens are indicated by red arrows. The larger scale 3.6μm image is shown in the upper left corner.

In the case of spiral arms, r_i and r_o refer to the inner and outer radius at which the different arms where measured, and α is the fitted pitch angle (positive/negative values distinguish between z- or s-type winding in the sky). The spiral quality flag refers to our visual estimation of the measurement quality (1.0 = good, 2.0 = acceptable). Highly uncertain cases in which the spiral arms are too hard to identify were not measured. The spiral arm classes are indicated by the letters G, F, and M for grand design, flocculent, and multiple types, respectively. For a subsample of S^{4}G galaxies this classification was done by Elmegreen et al. (2011), and for the complete sample by Buta et al. (2015), which is also the origin of the arm classes in our catalogue. The lower left panel shows again the 3.6 μm image in the sky plane, with the fitted spiral arm segments plotted on top of the image. The lower right panel shows the same image in logarithmic polar coordinates after deprojection to disk plane. The assumed disk orientation is from P4, and is indicated with the dashed ellipse in the left panel; these values are also shown in the title of the right panel.

4.1. Unsharp mask images

Inspecting the unsharp mask images forms part of our process of measuring the rings and spiral arms. Our unsharp masks are made by convolving the images with a Gaussian kernel, and then dividing the original image with the convolved image. The width of the Gaussian kernel vary from 3 to 50 pixels. In order to find the best way of seeing the structures in the images, the magnitude range of displaying the mask image is varied. With this convolution method we avoid possible artificial structures that might appear if the original images are simply divided by the re-

binned images. The unsharp mask images are shown for all the S^{4}G galaxies in the above described catalogue pages.

4.2. Barlengths

4.2.1. Measurements

Barlengths are estimated visually for all those barred galaxies in S^{4}G for which the end of the bar can be recognized in the 3.6 μm image, which also includes the high inclination galaxies. A vast majority of the galaxies with inclinations of $i < 65°$ are further measured using the ellipticity maximum in the bar region as a second proxy for the bar length. The nuclear and primary bars are measured in a similar manner.

In the visual barlength estimation the galaxies are first displayed in the screen with a chosen optimal brightness scale. Then one of the end points of the bar is marked, and a line connecting the bar ends is displayed (the bar is assumed to be symmetric with respect to the galaxy centre). This line is interactively stretched and rotated to match the bar in size and orientation, giving our visual barlength and position angle estimate. Naturally, in case of offset bars (16 galaxies) the centre of the bar was not the same as the galaxy centre. Uncertain barlength measurements (flag=3) appear in Table 2, but they are excluded from all the analyses in this paper. Another measure of the barlength is obtained from the P4 ellipticity profiles[2] The ellipticity and position angle profiles are displayed, and the location of the visually estimated barlength is marked on the graphs. The ellipticity maximum associated with the bar is then marked on these profiles and stored. The barlength measurements were made by two people (MHE and SDG), each of whom measured half of the galaxies. About 100 galaxies were measured by both people: based on these overlapping 'training' galaxies it was checked that the two independent estimates gave consistent results. With the remaining galaxies, both persons went through all the measurements and, if necessary, the measurement was made again after reaching an agreement on the interpretation of the bar for the galaxy in question.

Using the ellipticity maxima for measuring barlengths is a well-known approach (Wozniak & Pierce 1991). In an ideal case the ellipticity increases in the bar region, typically having a maximum at the end of the bar, after which it suddenly drops. In the bar region the position angle is maintained nearly constant. It has been suggested that the ellipticity maximum gives a lower limit of barlength (Athanassoula 2005). As an alternative, the length halfway between the maximum ellipticity in the bar region, and the first minimum after that maximum have been used (Erwin 2005). However, in S^{4}G and in galaxies more generally, such ideal cases are not very common. In fact, there are many barred galaxies in which no clear drop is visible after the maximum ellipticity. Therefore, in this study only the maximum ellipticity is used to measure the barlength (besides the visual estimate).

Sometimes prominent spiral arms starting at the two ends of the bar cause an additional ellipticity maximum; these spiral arms may also extend the radial region of a nearly constant position angle. In our approach this effect can be largely eliminated by inspecting simultaneously the images and the radial profiles of the ellipticity and position angle. The chosen ellipticity maximum is restricted to the obvious bar region, and local variations in the ellipticity profile give indications of possible spiral arms. However, it is not possible to eliminate the effect of the spiral

---

[2] The isophotal fits were recalculated for 70 barred galaxies in which the P4 ellipticity profiles, made with the purpose of determining the outer disk isophotal shape, failed to converge in the bar region.

Table 2. Properties of bars, ring- and lens-structures in the S^{4}G.

Galaxy	Classification (Buta et al. 2015)	Feature	a_{sky} (arcsec)	PA_{sky} (deg)	ϵ_{sky}	$a(\epsilon)_{sky}$ (arcsec)	a_{disk} (arcsec)	PA_{disk} (deg)	ϵ_{disk}	$a(\epsilon)_{disk}$ (arcsec)	Quality
ESO012-010	SAB(s)d	bar	14.0	21	0.50	12.3	27.3	43	0.71	23.1	1
ESO012-014	S/IB(s)m	bar	23.8	5	-	-	-	-	-	-	3
ESO013-016	SB(rs)cd	bar	16.1	166	0.75	13.8	16.1	167	0.61	13.8	1
ESO013-016	SB(rs)cd	rs	24.0	157	0.25	-	27.8	90	0.15	-	1
ESO015-001	IB(s)m	bar	14.3	120	-	-	-	-	-	-	2
ESO026-001	(R$_2'$)SAB(s)cd	bar	18.5	59	0.61	28.8	19.0	61	0.61	29.5	1
ESO026-001	(R$_2'$)SAB(s)cd	R$_2'$	38.4	54	0.32	-	39.3	59	0.31	-	2
ESO027-001	SAB(s)bc	bar	13.1	35	0.53	18.6	13.8	45	0.46	21.4	1
ESO027-008	SAB(s)bc	bar	14.8	131	-	-	-	-	-	-	1
ESO048-017	SB(s)m	bar	27.9	58	-	-	-	-	-	-	3
ESO054-021	(R')SAB(s)dm pec	bar	9.0	69	-	-	-	-	-	-	2
ESO054-021	(R')SAB(s)dm pec	R'	94.3	102	0.50	-	114.8	143	0.31	-	3
ESO079-005	SB(s)m	bar	15.6	13	0.82	19.1	17.7	27	0.76	21.8	2
ESO079-007	SB(s)dm	bar	13.9	24	0.64	14.4	14.0	26	0.56	14.4	2
ESO085-014	SBm	bar	23.5	74	-	-	-	-	-	-	2
ESO085-047	SB(s)m	bar	14.8	43	-	-	-	-	-	-	2
ESO107-016	SAB(s)dm sp	bar	7.4	98	-	-	-	-	-	-	3
ESO114-007	S/IAB(s)m / clump group	bar	13.0	78	-	-	-	-	-	-	3
ESO115-021	SAB(s)m sp	bar	23.4	47	-	-	-	-	-	-	3
ESO116-012	SAB(s)m sp	bar	24.0	33	-	-	-	-	-	-	3
ESO119-016	(R')SAB(s)dm:	bar	15.6	57	-	-	-	-	-	-	3
ESO119-016	(R')SAB(s)dm:	R'	68.6	30	0.75	-	71.7	48	0.36	-	3
ESO120-012	IAB(s)m	bar	24.5	96	-	-	-	-	-	-	3
ESO145-025	SAB(s)dm	bar	12.0	156	-	-	-	-	-	-	3
ESO149-001	SB(s)d sp	bar	17.0	32	-	-	-	-	-	-	3
ESO154-023	SB(s)dm sp	bar	46.4	36	-	-	-	-	-	-	3
ESO187-035	SB(s)m	bar	22.1	116	-	-	-	-	-	-	3
ESO187-051	SAB(s)m	bar	12.3	17	-	-	-	-	-	-	3
ESO202-041	SAB(rs)m	bar	17.1	166	-	-	-	-	-	-	2
ESO202-041	SAB(rs)m	rs	25.3	173	0.09	-	34.4	239	0.27	-	3
ESO234-043	SAB(s)dm:	bar	18.7	57	0.68	24.0	22.3	43	0.66	28.8	2
ESO234-049	SA(r)cd pec	r	8.1	165	0.58	-	8.8	165	0.61	-	1
ESO236-039	S/IABm:	bar	10.0	93	0.62	14.3	10.9	119	0.32	15.9	2
ESO237-052	SAB(s)dm:	bar	13.2	47	0.48	15.6	16.0	1	0.12	17.2	2
ESO238-018	SAB(s)dm	bar	6.9	138	0.68	6.8	7.3	135	0.69	7.3	1
ESO245-005	S/IAB(s)m	bar	50.3	118	-	-	-	-	-	-	3
ESO248-002	(L)SB(s)d	bar	25.8	26	-	-	-	-	-	-	2
ESO248-002	(L)SB(s)d	L	85.0	13	0.77	-	85.8	-10	0.06	-	1
ESO249-035	SB(s)dm sp	bar	20.6	96	-	-	-	-	-	-	3
ESO285-048	SB(rs)d	bar	10.2	102	0.75	17.2	13.2	128	0.64	20.9	1
ESO285-048	SB(rs)d	rs	21.3	70	0.64	-	24.5	39	0.35	-	2
ESO287-037	SAB(s)dm	bar	18.7	163	0.40	21.1	20.6	159	0.45	22.8	2
ESO287-043	SAB(s)m sp	bar	18.6	105	-	-	-	-	-	-	3
ESO288-013	SAB(s)dm	bar	15.9	35	0.62	17.2	16.2	32	0.61	17.9	2
ESO289-026	SAB(s)d	bar	26.9	118	0.77	33.7	38.4	96	0.77	49.6	2
ESO289-048	SAB(s)d sp	bar	17.2	153	-	-	-	-	-	-	3
ESO298-015	SAB(s)dm	bar	14.0	43	-	-	-	-	-	-	2
ESO298-023	S/IABm:	bar	10.6	51	-	-	-	-	-	-	3
ESO302-021	SB(s)m sp	bar	16.2	5	-	-	-	-	-	-	3

Notes. Data for bars contains the visual estimated barlength (a), the maximum ellipticity in the bar region (ϵ), the visual estimated position angle (PA), and the barlength obtained from the ellipticity maximum ($a(\epsilon)$). They are given in both the sky plane and the disk plane, the conversion is made using P4 orientation parameters (Salo et al. 2015; Table 1). For bars the disk plane values are given only when a reliable ellipticity maximum was found and the galaxy inclination $i < 65°$. For other features the parameters are obtained from fitting ellipses to points tracing the structure. A quality flag for our measurement is also given: 1 indicates a good fit and unambiguously identified feature, 2 indicates a hard to trace feature, 3 indicates an uncertain feature identification (due to high inclination of host galaxy or incomplete feature).

arms in galaxies where, instead of causing a separate ellipticity maximum, the spiral arms just make the ellipticity gradually increase up to the distance where the spiral arms dominate. There are also galaxies where no clear maximum appears in the ellipticity profile. In such cases we take a conservative approach and do not measure the length of the bar, which is the case mainly

among the lower luminosity galaxies at the end of the Hubble sequence.

Two examples of our barlength measurements are shown in Figure 4. NGC 5375 represents an ideal case where a clear ellipticity maximum appears. The radius of this maximum gives the same barlength as estimated visually ($r=27$"). The position angle is maintained nearly constant to $r=32$", and the first min-

Table 3. Properties of spiral arms in the S^{4}G.Type of spiral arms, the pitch angle (α), the inner (r_i), and the outer radius (r_o) are given for every spiral segment (see the catalogue web page). The type of spiral arms are taken from Buta et al. (2015): G for grand design, M for multiple, and F for flocculent spiral arms. Our estimation of the quality of the fit is also given (1.0 = good; 2.0 = acceptable).

Galaxy	Classification (Buta et al. 2015)	Type (Buta et al. 2015)	Segment	α (deg)	r_i (arcsec)	r_o (arcsec)	Quality
ESO 012-010	SAB(s)d	F	sp1	-40.8	33.2	93.4	1.0
ESO 012-010	SAB(s)d	F	sp2	-32.2	37.3	90.4	1.0
ESO 026-001	(R$'_2$)SAB(s)cd	M	sp1	-13.3	26.5	47.2	2.0
ESO 026-001	(R$'_2$)SAB(s)cd	M	sp2	-12.0	24.9	49.1	2.0
ESO 027-001	SAB(s)bc	M	sp1	36.9	21.2	38.1	1.0
ESO 027-001	SAB(s)bc	M	sp2	5.7	39.9	46.4	1.0
ESO 027-001	SAB(s)bc	M	sp3	28.7	48.4	110.6	1.0
ESO 027-001	SAB(s)bc	M	sp4	2.9	112.4	120.0	1.0
ESO 027-001	SAB(s)bc	M	sp5	15.2	29.3	109.1	1.0
ESO 027-008	SAB(s)bc	G	sp1	17.2	22.5	67.3	1.0
ESO 027-008	SAB(s)bc	G	sp2	10.4	23.3	39.5	1.0
ESO 027-008	SAB(s)bc	G	sp3	30.1	41.3	79.4	1.0
ESO 027-008	SAB(s)bc	G	sp4	48.6	29.4	85.1	1.0
ESO 054-021	(R$'$)SAB(s)dm pec	F	sp1	28.9	26.4	139.1	2.0
ESO 054-021	(R$'$)SAB(s)dm pec	F	sp2	29.6	34.2	153.5	2.0
ESO 116-012	SAB(s)m sp	F	sp1	-8.6	61.1	84.3	2.0
ESO 116-012	SAB(s)m sp	F	sp2	-58.5	21.0	59.9	2.0
ESO 238-018	SAB(s)dm	F	sp1	-7.0	17.8	24.5	2.0
ESO 238-018	SAB(s)dm	F	sp2	-40.9	9.0	14.9	2.0
ESO 287-037	SAB(s)dm	F	sp1	8.2	36.6	47.5	2.0
ESO 287-037	SAB(s)dm	F	sp2	7.9	33.3	38.4	2.0
ESO 288-013	SAB(s)dm	F	sp1	-7.8	26.9	37.0	2.0
ESO 288-013	SAB(s)dm	F	sp2	-1.2	36.9	37.9	2.0
ESO 288-013	SAB(s)dm	F	sp3	-27.2	15.8	38.3	2.0
ESO 289-026	SAB(s)d	G	sp1	28.8	46.9	92.5	2.0
ESO 289-026	SAB(s)d	G	sp2	39.2	36.4	88.9	2.0
ESO 340-042	SB(s)dm	F	sp1	-31.8	20.9	62.3	2.0
ESO 340-042	SB(s)dm	F	sp2	-46.4	18.9	33.2	2.0
ESO 340-042	SB(s)dm	F	sp3	-22.8	33.8	59.3	2.0
ESO 340-042	SB(s)dm	F	sp4	-4.1	60.2	64.0	2.0
ESO 342-050	SA(s)bc	M	sp1	-32.2	13.0	30.8	1.0
ESO 342-050	SA(s)bc	M	sp2	-19.6	30.3	87.7	1.0
ESO 342-050	SA(s)bc	M	sp3	-33.6	20.4	80.8	1.0
ESO 342-050	SA(s)bc	M	sp4	-15.5	25.4	50.6	1.0
ESO 355-026	SA(r)bc	M	sp1	-11.9	17.0	49.0	2.0
ESO 355-026	SA(r)bc	M	sp2	-18.0	14.2	38.4	2.0
ESO 355-026	SA(r)bc	M	sp3	-60.9	19.4	36.3	2.0
ESO 355-026	SA(r)bc	M	sp4	-14.2	38.0	43.9	2.0
ESO 404-027	SAB(s)ab:	G	sp1	21.4	24.2	64.2	1.0
ESO 404-027	SAB(s)ab:	G	sp2	5.8	65.4	83.0	1.0
ESO 404-027	SAB(s)ab:	G	sp3	14.2	29.2	60.9	1.0
ESO 407-009	SA(s)bc	M	sp1	-20.2	23.9	86.8	2.0
ESO 407-009	SA(s)bc	M	sp2	-7.7	29.9	41.8	2.0
ESO 440-011	SB(rs)cd	M	sp1	-42.2	34.6	84.8	2.0
ESO 440-011	SB(rs)cd	M	sp2	-15.1	85.7	106.9	2.0
ESO 440-011	SB(rs)cd	M	sp3	-19.0	34.4	59.8	2.0
ESO 443-069	(R$'$)SB(rs)dm	M	sp1	-8.3	36.3	45.4	2.0
ESO 443-069	(R$'$)SB(rs)dm	M	sp2	-38.1	26.7	55.6	2.0
ESO 443-069	(R$'$)SB(rs)dm	M	sp3	-7.1	57.5	80.0	2.0
ESO 443-069	(R$'$)SB(rs)dm	M	sp4	-26.7	45.1	73.5	2.0
ESO 443-085	SB(s)d	M	sp1	-19.8	22.8	45.0	2.0
ESO 443-085	SB(s)d	M	sp2	-17.9	21.5	42.1	2.0
ESO 485-021	SAB(s)cd	G	sp1	50.3	32.5	66.0	2.0
ESO 485-021	SAB(s)cd	G	sp2	13.0	73.2	98.3	2.0
ESO 485-021	SAB(s)cd	G	sp3	46.5	32.6	66.7	2.0
ESO 485-021	SAB(s)cd	G	sp4	12.6	68.3	96.8	2.0

imum after the ellipticity maximum appears at $r \approx 40''$. Looking at the image it is clear that at $r=40''$ the spiral arms are already dominating. The position angle is maintained constant even after the ellipticity maximum, which in this galaxy could give an upper limit of the barlength. In NGC 4314 the bar is strong, but has no clear maximum in its ellipticity profile, instead a broad bump appears. The visual barlength corresponds to the radius where the spiral arms start on both sides of the bar. The strong spiral arms prevent the position angle profile from changing, which is almost constant up to $r = 100''$. In these cases we looked at the
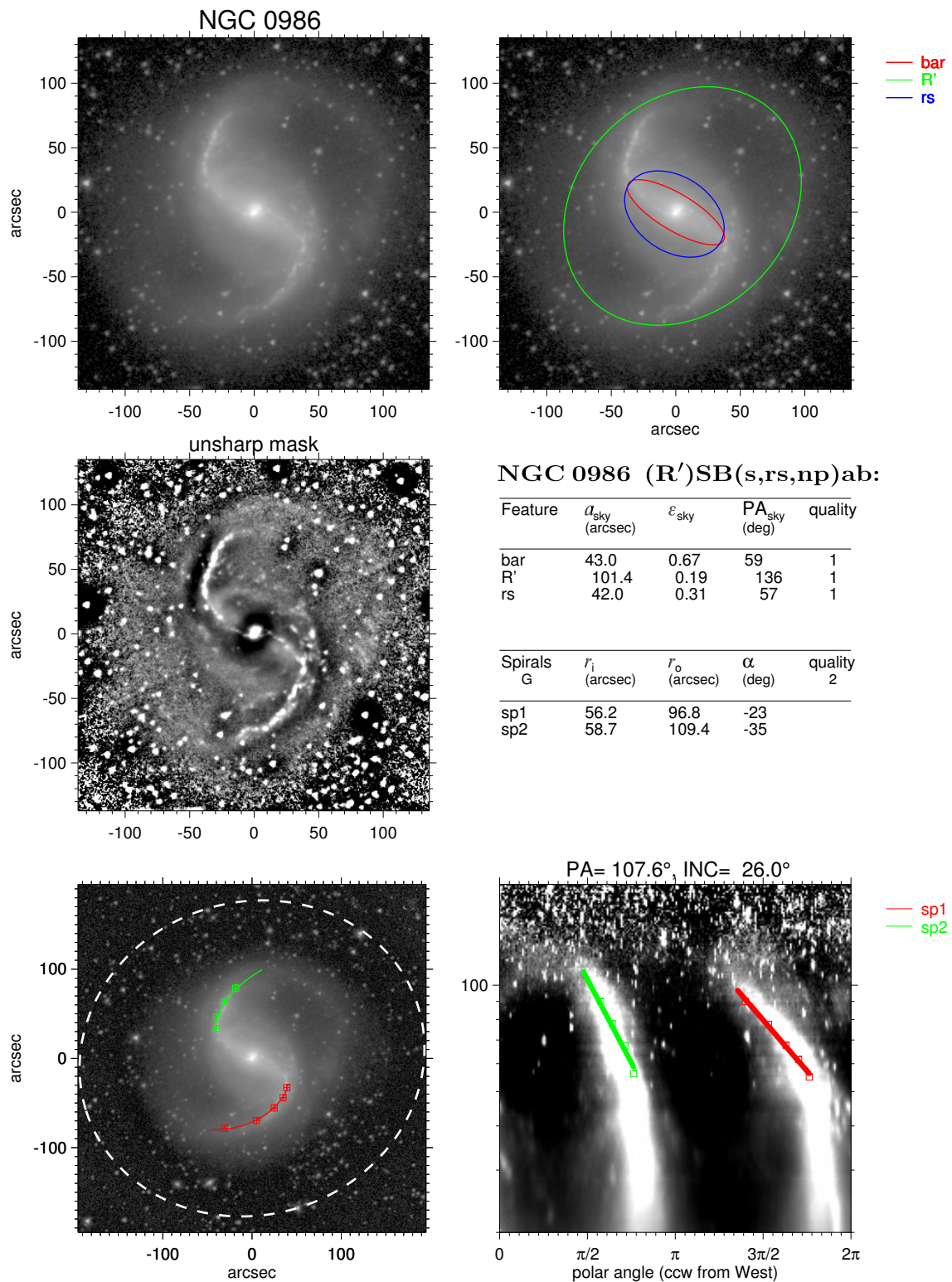
NGC 0986

unsharp mask

NGC 0986 $(R')SB(s,rs,np)ab$:

Feature	a_{sky} (arcsec)	ε_{sky}	PA_{sky} (deg)	quality
bar	43.0	0.67	59	1
R'	101.4	0.19	136	1
rs	42.0	0.31	57	1

Spirals G	r_i (arcsec)	r_o (arcsec)	α (deg)	quality 2
sp1	56.2	96.8	-23	
sp2	58.7	109.4	-35	

PA= 107.6°, INC= 26.0°

Fig. 3. An example galaxy from our catalogue web page. The panels are explained in the text.

image and the small variations in the ellipticity profile to decide the size of the bar.

Of the 1174 bars in the classification by Buta et al. (2015), we measured the lengths for 1146 of them visually. Of these measurements 830 were considered reliable (e.g. quality flag=1 or 2 in Table 2). The number of barred galaxies with inclinations $i < 65°$ in S^{4}G is 900, of which barlengths from the ellipticity maximum were measured for 653 galaxies. Finally, the measurements were converted from the sky plane values to the disk plane, using the P4 orientation parameters.
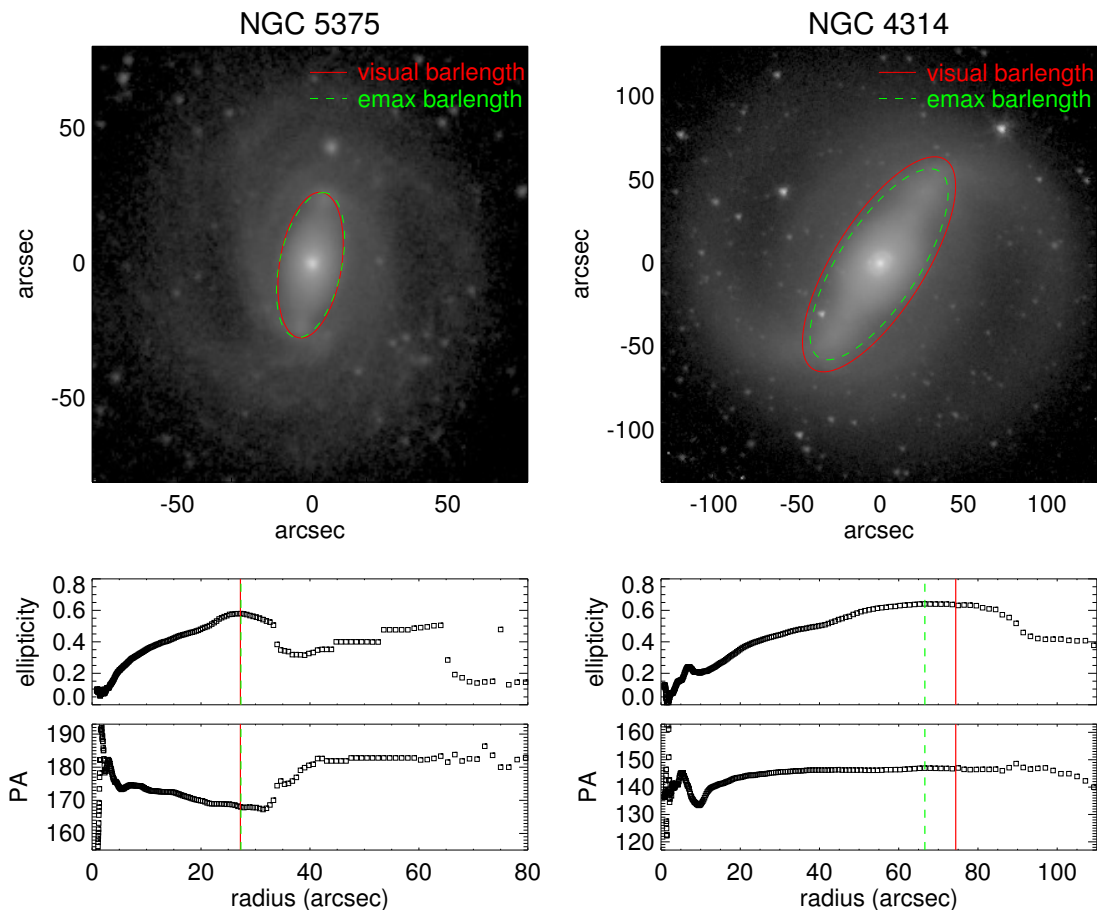
Fig. 4. Two examples (NGC 5375 and NGC 4314) of barlength measurements, based on visual estimation (red continuous line), and on ellipticity maximum (green dashed line). The bottom panels show the radial profiles of the ellipticity and position angle. Indicated with the vertical lines are the barlength measurements based on the two approaches.
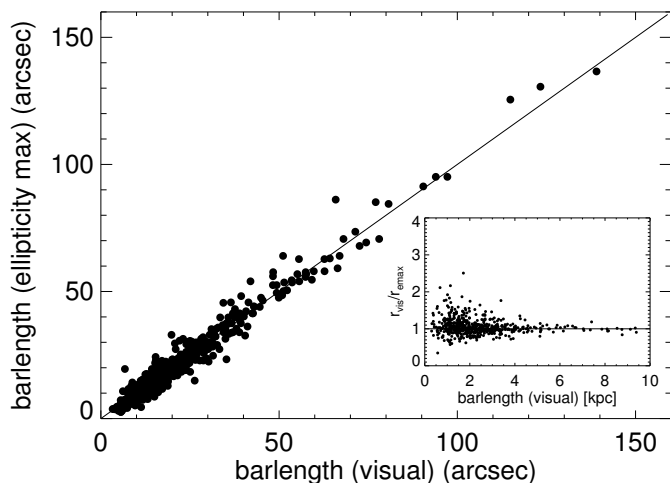
Fig. 5. A comparison of the barlength measurements, based on the two approaches used. Only galaxies with $i < 65°$ and with a reliable ellipticity maximum are shown. The insert shows the deviations from the unit ratio.

4.2.2. Comparison of the two barlength measurements

A comparison of our two barlength measurements is shown in Figure 5. Bars with inclinations smaller than 65° and also having a reliable ellipticity maximum in the bar region were selected. There is some scatter in the plot, but no systematic difference appears between the visually obtained barlengths and those measured from the maximum ellipticity in the bar region. This is not surprising, considering that the galaxies were treated individually so that both measurements generally avoid possible problems related to spiral arms or rings at the two ends of the bar. Dust lanes are expected to affect the measurements in the optical region, but not in our measurements using the mid-IR images.

However, the fact that our two barlength measurements are in a fairly good agreement with each other does not yet mean that the scatter reflects just a random measurement uncertainty. In fact, no single approach can give exactly the right measurement for all bars, but we have to live with this uncertainty. Bars have different morphologies, from regular elongated structures to bars with prominent ansae at the two ends of the bar. It is clear that such bars also have different intensity profiles, which might slightly affect the location of the ellipticity maximum, independent of where the bar ends. However, because the deviations between our two measurements are very small, we can be confident that the lengths of bars are measured in a consistent manner for all galaxies in S^{4}G.
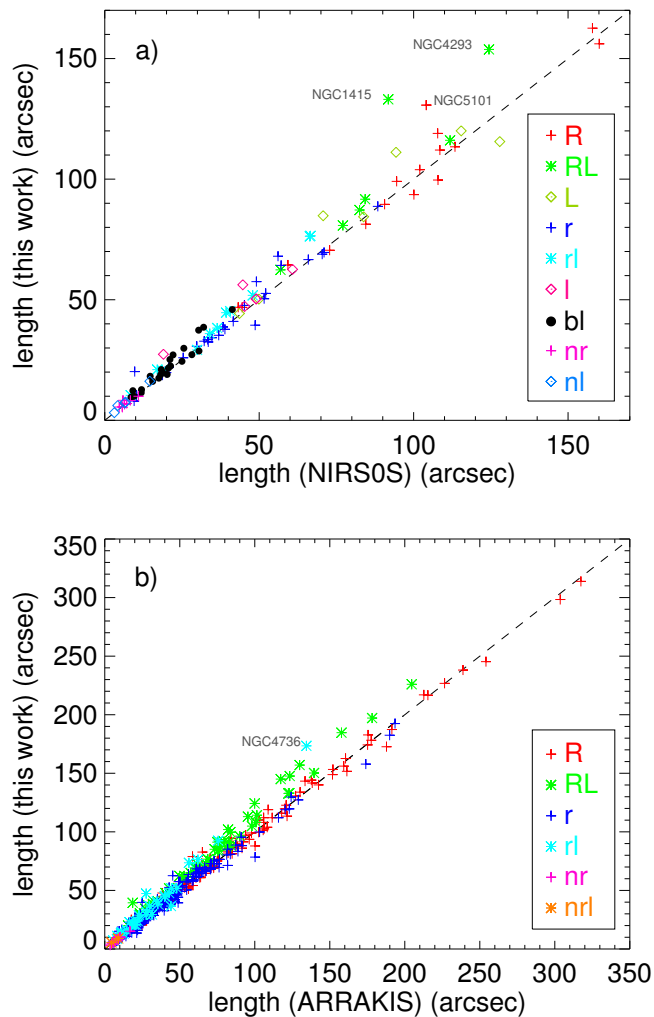
Fig. 6. Our size measurements of the different structure components are compared with those previously obtained for (a) the galaxies in NIRS0S at 2.2μm (Laurikainen et al. 2011), and (b) in ARRAKIS at 3.6μm (Comerón et al. al 2014). The galaxies for which the measurements deviate more than 20" are indicated by name.

4.3. Dimensions and ellipticities of the rings, ringlenses, and lenses

For the measurements of the dimensions, ellipticities, and orientations of the nuclear, inner and outer rings, ringlenses, and lenses we use a procedure in which the image of a given galaxy is displayed on the screen, and then the structure is visually marked. The brightness scale and image range are both adjusted to give optimal visibility of the structure. An ellipse is then analytically fitted on the marked points. In the case of lenses and ringlenses the edges of the structures are marked, whereas for rings the ridge-line is traced. The fit gives the central coordinates, the orientations, and the semi-major and semi-minor axis radii of the feature. This fitting procedure is repeated three times for each structure, and the mean value is used. For 900 structures we also experimented with fits where the centre of the feature was fixed to be the same as that of the galaxy. These measurements were then compared with our original measurements, where such a requirement was not made. Features that were clearly off-centred or uncertain were excluded. We found

that the mean absolute deviations in the semi-major and semi-minor axis lengths and the position angle were 0.48″, 0.33″, and 4.4°, respectively. Clearly, for the first two parameters the deviations are not much higher than the resolution of the images.

As rings are generally sharper than lenses or ringlenses, their visibility in the images can be further improved using the unsharp mask images. Therefore, instead of using the original images, rings are identified and measured using the unsharp mask images. In particular, this allows us to better identify nuclear rings, which are easily overshadowed by the luminous bulges. Also, nuclear rings are often regions of strong star formation, which in the optical region are easily obscured by dust. However, for the lack of dust extinction at 3.6 μm wavelengths they are easily visible via the PAH emission lines typical in star forming regions.

Although barlenses are not lenses in the same sense as the other lenses in galaxy classification, their sizes are measured in a similar manner. By definition, barlenses appear only in barred galaxies. Furthermore, they appear only in fairly bright galaxies, which means that they are absent in Hubble types later than Sc.

4.4. Comparison with NIRS0S and ARRAKIS

Comparison with NIRS0S. To ensure that we have measured the dimensions of the features in a similar manner as in the previous studies, our measurements are compared with those given in the Near-IR S0 galaxy Survey by Laurikainen et al. (2011, hereafter NIRS0S), in which dimensions of rings, ringlenses, lenses, and barlenses, in a sample of ~200 early-type disk galaxies were measured. They used K_s-band images typically reaching surface brightnesses of 23.5 mag arcsec^{-2} in the K_s-band, roughly equivalent to 27.5 mag arcsec^{-2} in the B-band. In S^{4}G there are 93 galaxies in common with NIRS0S. For each galaxy we selected the structures that correspond to the same classifications in NIRS0S and in S^{4}G, which makes 105 features in 61 galaxies (not all galaxies have rings or lenses, and not all outer structures are identified in NIRS0S). The comparison of the sizes is shown in Figure 6a.

There is a good agreement between our measurements and those given in NIRS0S, except for three measurements that differ by more than 20". The structures are RL in NGC1415 and NGC4293 and R in NGC5101. In all three galaxies we associate the difference in size with the different image depths in the two samples: the images are deeper in S^{4}G thus allowing the outer structures to be traced more accurately.

Comparison with ARRAKIS. Another source of reference is the atlas of resonance rings by Comerón et al. (2014, hereafter ARRAKIS) for a large sample of galaxies in S^{4}G. However, in ARRAKIS lenses and barlenses were not measured. Although both studies use the S^{4}G sample, the identification of the structures in ARRAKIS and this study might vary a little because ARRAKIS used Buta's Phase 1/Phase 2 classifications, while we use the final classifications in Buta et al. (2015). This explains the small difference in the number of rings in bright galaxies between the two studies. There is also a small difference in the way the measurements were done. In ARRAKIS residual images after subtracting the decomposition models were used. The residual images were taken from the P4 decompositions (Salo et al. 2015) in which bulges, disks, and bars were fitted with separate functions. Ellipse fitting was then done to the residual images. This is not much different from our approach where unsharp mask images were used instead. However, in principle our approach
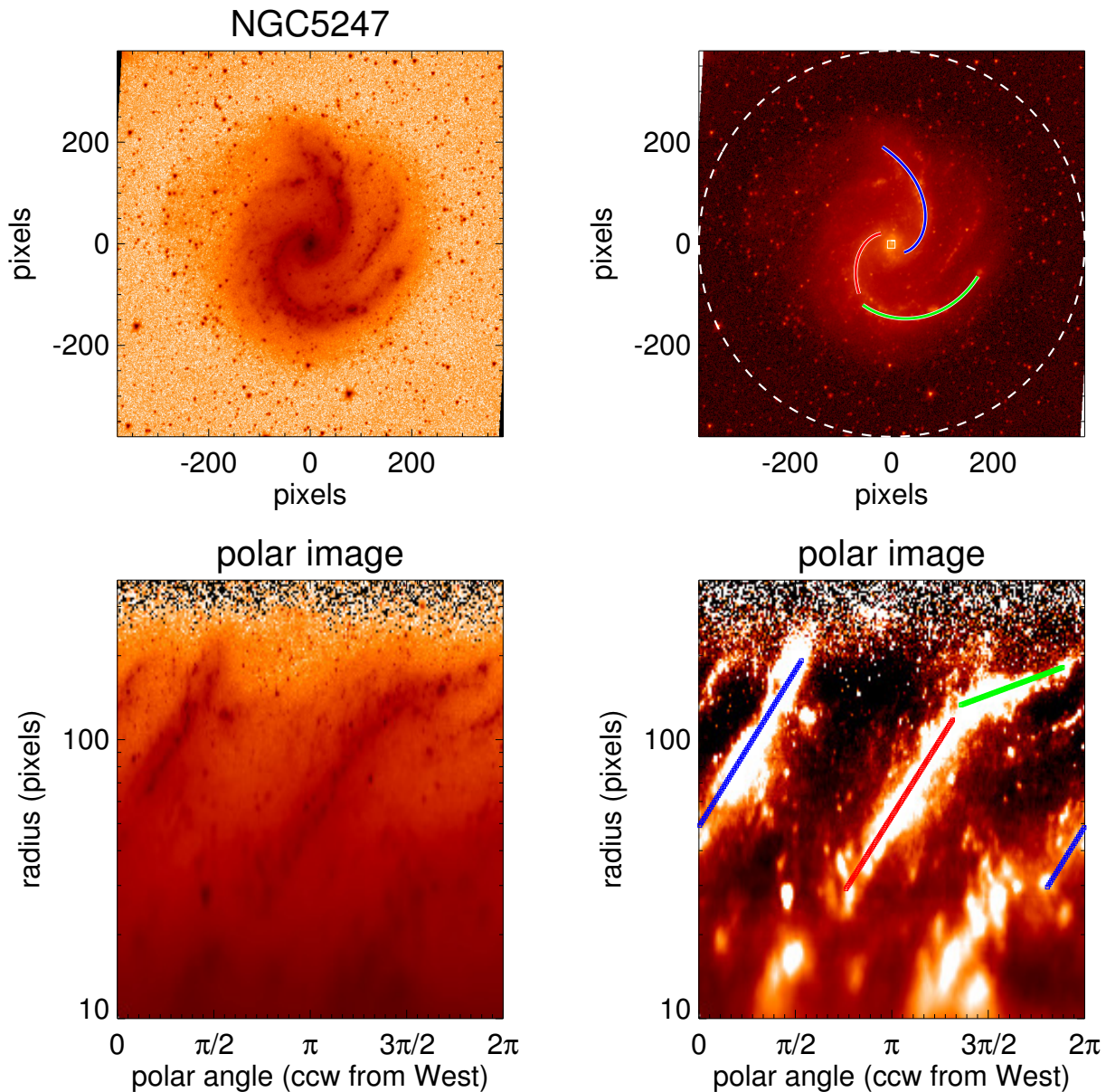
Fig. 7. An example for NGC 5247 of our measurements of the spiral arms. The upper panels show the original 3.6 μm image. The lower left panel shows the same image in polar coordinates, and the lower right panel an unsharp mask image, also in polar coordinates. In the right panels the locations of the measured spiral arms are indicated. The different colours of the lines show the spiral arm segments that were fitted with different pitch angles.

is safer because decomposition residuals may contain artificial structures at faint levels.

In order to compare our measurements with those made in ARRAKIS, common galaxies between the two studies were selected, concentrating on galaxies where the classifications were the same in both studies; this makes 1324 features in 724 galaxies (see Figure 6b). In general there is a very good agreement in the sizes: the median difference is 1.1″ with the mean absolute deviation of 2.8″. Some differences in ringlenses (e.g. rl in NGC 4736 marked in 6b) can arise because we measured the structures from the outer edges, whereas in ARRAKIS they were measured from the ridge-lines.

4.5. Pitch angles of the spiral arms

The spiral arms are measured for all galaxies in S⁴G, except for the clumpy irregular galaxies at the end of the Hubble sequence. The fast Fourier transform method is often used to identify spiral arms and to measure their pitch angles (Saraiva Schroeder et al. 1994; Seigar et al. 2005; Davis et al. 2012). This method reconstructs the spiral arms in an efficient manner, based on the different Fourier amplitudes of density associated with two- or multi-armed spiral patterns. Drawbacks of this method are discussed by Elmegreen et al. (1992). For example, the higher Fourier modes do not always trace real three- or four-armed spiral patterns in galaxies. For asymmetric spiral arms a specific method of measuring the pitch angles is developed by Elmegreen et al.

(1992). It is based on highlighting the spiral arms by making image rotation and subtracting different galaxy components from the original images. These methods are generally used in such a manner that only one pitch angle is given for each galaxy.

However, we adopted a different approach, based on visual inspection of the spiral arms, in the same spirit as the other measurements of this study. This is the first step of our analysis of the spiral arms, allowing the identification of several pitch angles at different radial distances in galaxies, and taking into account that those pitch angles might appear asymmetrical with respect to the galaxy centre. An important part of our analysis is to display arms in polar coordinates which easily identifies deviations from logarithmic spirals, and therefore also highlights the segments with distinct pitch angles in galaxies.

Again, the fitting procedure is interactive: the unsharp mask images are displayed in different scales in order to see the spiral arms clearly, after which the spiral arms are marked. The marked points are then displayed on top of the deprojected galaxy image using logarithmic polar coordinates, where the logarithmic spirals appear as straight lines. From this plot the points belonging to different, roughly logarithmic arm segments are selected, and fitted with a line. The pitch angle of this segment, together with the minimum (r_i) and maximum (r_o) radial range of the fit are then stored. An example of our measurements is given in Figure 7. The obtained pitch angles and the radial ranges of the measurements are given in Table 3 and the catalogue web pages. Note that we did not perform any new classification of the spiral arms; instead the classifications by Elmegreen et al. (2011) and Buta et al. (2015) are shown.

5. Analysis and discussion

Bars identified in the classification by Buta et al. (2015) in S⁴G are used to study the properties of bars in several papers. The bar fractions were discussed by Buta et al. and Sheth et al. (2014). Barlength measurements obtained in this catalogue, combined with bar strength measurements, are analysed by Díaz-García et al. (2015). In this study we concentrate on the rings, ringlenses, lenses, and barlenses, and use barlength only as a normalization factor for the sizes of the other structure components. In the figures the visually estimated deprojected barlengths are used.

5.1. Resonant nature of rings, ringlenses, and lenses

Statistics of the features identified in the classification by Buta et al. (2015) were made in the original paper. For example it was shown that the fraction of inner rings is lowest in galaxies with the highest bar fraction. This is the case particularly for the very late-type galaxies (T≥6), which also have low baryonic masses and high gas fractions. A similar tendency was also found by Buta et al. for the S0s at the bright end of the mass distribution, in which lenses largely replace the rings. A drop in ring fraction, and an increase in lens fraction among the early-type S0s was also recognized by Laurikainen et al. (2009, 2013). However, in these studies it was not clear whether the lenses could also be interpreted as resonance structures, in a similar manner as the rings.

An important consequence of the presence of bars in disk galaxies is the appearance of dynamical resonances (Sellwood & Wilkinson 1993). The disk material collects into these resonances giving rise to the creation of rings (e.g. Schwarz 1981, 1984). The relevant resonances in this regard are the outer Lindblad resonance (OLR) located at a radius roughly two times that

of the bar, the inner ultraharmonic resonance (UHR) located slightly outside the bar radius, and the inner Lindblad resonances (ILRs) located well inside the bar [3]. As mentioned in Section 3, the outer, inner, and nuclear rings, respectively, are believed to be related to these resonances.

In order to study the resonant nature of the inner and outer rings we show their sizes normalized to the size of the bar. This is a useful normalization as the bar corotation radius is always within a factor of ~2 from the bar radius: a theoretical minimum is R_{cr}/R_{bar}=1, since bar supporting orbits are not possible beyond corotation. These normalizations thus makes it possible to exclude features which definitely are not bar-related phenomena. We concentrate on galaxies with Hubble stages T≤5, largely covering only the bright galaxies that have peaked central flux distributions. The inner rings are peaked to length/barlength ~1.0 (Fig. 8a), which is similar to the rings in NIRS0S. There is a tail towards the higher values which, for the larger number of galaxies in S⁴G, is even clearer than in NIRS0S.

The inner lenses and ringlenses have very similar sizes to the rings. For ringlenses this confirms the result obtained in NIRS0S. However, in NIRS0S lenses were found to be larger than the rings by a factor of 1.3. Whether this difference between NIRS0S and the current study is significant still needs to be confirmed by a larger sample of lenses. If real, it might be related to the fact NIRS0S contains gas-poor early-type S0s, which are missing in S⁴G. The (gas-poor) early-type S0s in NIRS0S are on average brighter than the later type S0s and early-type spirals in the same sample (see Laurikainen et al. 2011).

The outer features are illustrated in Figure 8b. For the outer rings we obtain a peak at length/barlength≈2.4, again in agreement with the previous studies (Kormendy 1979; Buta 1995; Laurikainen et al. 2013), and also with the predictions of the simulation models in case that the rings appear in the well-known resonances (see Schwarz 1981; Buta & Combes 1996). However, the peak is quite broad, possibly reflecting different mass distributions of the galaxies or the fact that the R_{CR}/R_{bar} ratio varies from galaxy to galaxy. It appears that the outer rings, ringlenses, and lenses have very similar length distributions, most probably indicating that they have similar physical origins.

In both panels of Figure 8 the distributions show tails towards large relative sizes of the structures. The relative sizes larger than 2.5 in Figure 8a (2 cases), or larger than 5 in Figure 8b (13 cases) are excluded from the subsequent figures and analysis. Although they seem to be correctly measured (flag = 1, 2 in Table 2), they are obviously not related to the resonances of bars.

5.2. Rings and lenses in different Hubble types and bar families

By bar strength we mean here simply the family class of the bar. It is generally assumed that strong bars are efficient in redistributing matter in galaxies towards the nuclear regions (Sellwood & Wilkinson 1993), and in accumulating gas into the resonances (Schwarz 1981). Curiously, it appears that weak (AB) bars rather than strong (B) bars are more efficient in collecting matter into the resonances where the inner rings appear, i.e. the fraction of inner rings is clearly larger among weakly barred

---

[3] For a flat rotation curve the linear treatment of resonances implies $R_{OLR}/R_{CR} = 1 + \sqrt{2}/2 \approx 1.7$, $R_{UHR}/R_{CR} = 1 - \sqrt{2}/4 \approx 0.65$, where R_{CR}, R_{UHR}, and R_{OLR} are the bar corotation, UHR, and OLR distances. Bars are generally assumed to end somewhat inside corotations, $1 < R_{CR}/R_{bar} < 1.7$. Using the nominal value $R_{CR}/R_{bar} = 1.4$ then gives $R_{OLR}/R_{bar} \sim 2.4$ and $R_{UHR}/R_{bar} \sim 0.9$.
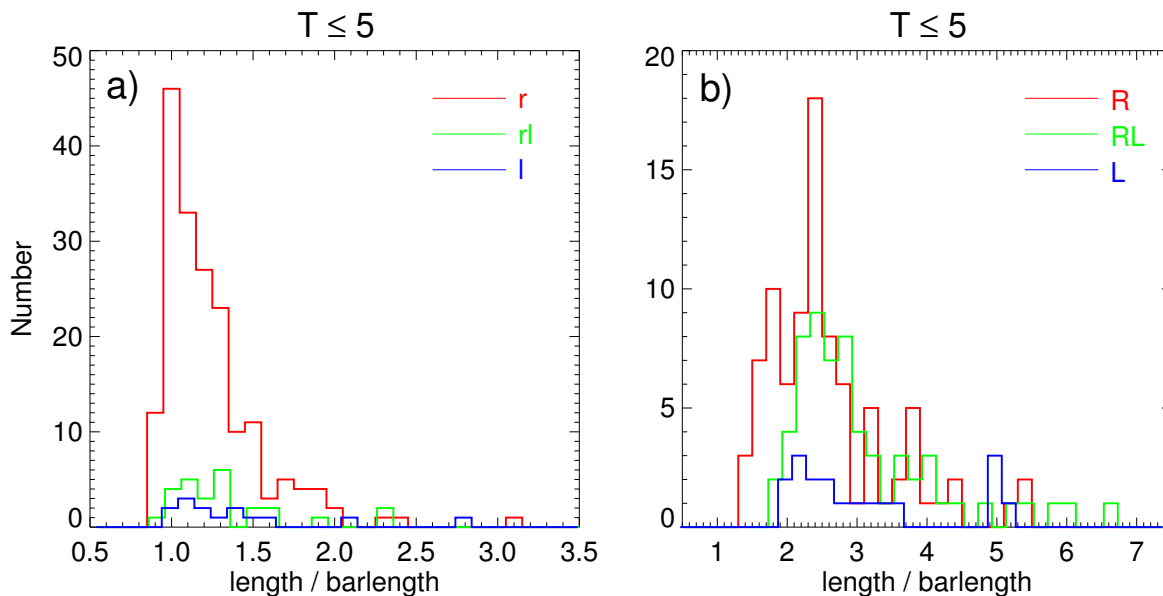
Fig. 8. The sizes of the different structure components in barred galaxies, normalized to the barlength. Only galaxies with Hubble types earlier than or equal to T=5 are shown. In (a) the inner and in (b) the outer features are displayed. The subtypes of all features are included for each type.

galaxies (see Fig. 9, upper middle panel). The found tendency is even clearer for the inner lenses. However, it is completely lacking for the outer and nuclear features. This tendency for the inner structures might be a manifestation of possible dissolution of bars into rings and lenses (see Kormendy 1979). However, so far there is no theoretical confirmation of this interpretation. Looking at the fractions of the features in different Hubble types, it appears that lenses and ringlenses are concentrated in the earlier morphological types (see Fig. 9, lower panel). The fraction of lenses increases towards the S0s, whereas the fraction of rings peaks at Sa Hubble types. This is the case both for the inner, outer, and nuclear features. Similar trends for the S0-Sa galaxies were also found in the NIRS0S atlas.

5.3. Effect of the parent galaxy mass on the measured features

5.3.1. Sizes normalized to barlength

The lengths of the rings, ringlenses, and lenses are shown as a function of galaxy stellar mass and morphological type in Figure 10. The lengths are normalized to the size of the bar, using the measurements converted to the disk plane. The stellar masses are taken from Muñoz-Mateos et al. (2013).

A clear correlation appears between the normalized size of the inner feature and the parent galaxy mass (Fig. 10a, green symbols). The shown correlation (the fitted line) is also statistically significant, and implies that the average size of the inner feature increases by about 50% when the galaxy stellar mass decreases from $10^{11} M_\odot$ to $10^9 M_\odot$. For the outer features (R, RL, L) the scatter is high and there is no clear trend visible. The scatter is particularly high for the nuclear features (nr, nrl, nl), but an interesting characteristic for these features is that they appear only above a parent galaxy mass $M > 10^{10} M_\odot$. Since the low mass galaxies are not centrally peaked it means that bars in those galaxies are not likely to have an inner Lindblad resonance (ILR), which could collect gas into the nuclear rings. Indeed, based on the structural decompositions, it has been shown by

Salo et al. (2015) that the relative mass of the central concentration in the S⁴G galaxies rapidly drops below $10^{10} M_\odot$. This mass limit roughly corresponds to the Hubble stage T=5. Figure 10b shows the sizes of the same features as a function of Hubble type. It appears that the nuclear features and barlenses appear only in Hubble stages T < 5.

In principle an increasing mass concentration in barred galaxies is expected to push the resonances of bars to larger radial distances (Schwarz 1981; Combes & Gerin 1985; Contopoulos 1980). With an increasing mass concentration the co-rotation radius of the bar increases, and as the bar tries to follow the co-rotation radius, barlength also increases. Consequently, the inner and outer rings associated with the inner 1/4 ultra-harmonic (UHR) and outer Lindblad (OLR) resonances would also be pushed further away from the galaxy centre. Therefore, it is not immediately obvious why the normalized sizes of the resonance features decrease towards the higher parent galaxy masses.

In order to better understand the observed trend of the inner ring sizes we can look at the simulation models for IC 4214 (Salo et al. 1999), where detailed comparisons of the observed morphological and kinematic properties of this prototypical galaxy (with M= $5 \cdot 10^{10} M_\odot$) were made based on an extensive series of simulations. The simulations addressed the response of sticky-particle 'gas' on a rigidly rotating bar potential using various pattern speeds and bar amplitudes. The galaxy potential was obtained from the *H*-band image (Buta et al. 1999), and the nominal bar amplitude $A = 1$ corresponded to total potential derived directly from the image. A value of $A < 1$ would imply that part of the axisymmetric force field is due to a spherical dark matter halo (or additionally that the density contrast related to the bar is less than implied by the flux contrast). It was found (see their Table 1) that the simulated ring sizes, for a given pattern speed, depend strongly on the bar amplitude A. For the best fitting amplitude (A=0.75) the inner ring radius was coincident with the estimated bar length. However, decreasing the amplitude from $A = 0.75$ to $A = 0.33$ increased the inner ring radius by about $\sim 10\%$. Such a reduction would be at least qualitatively con-
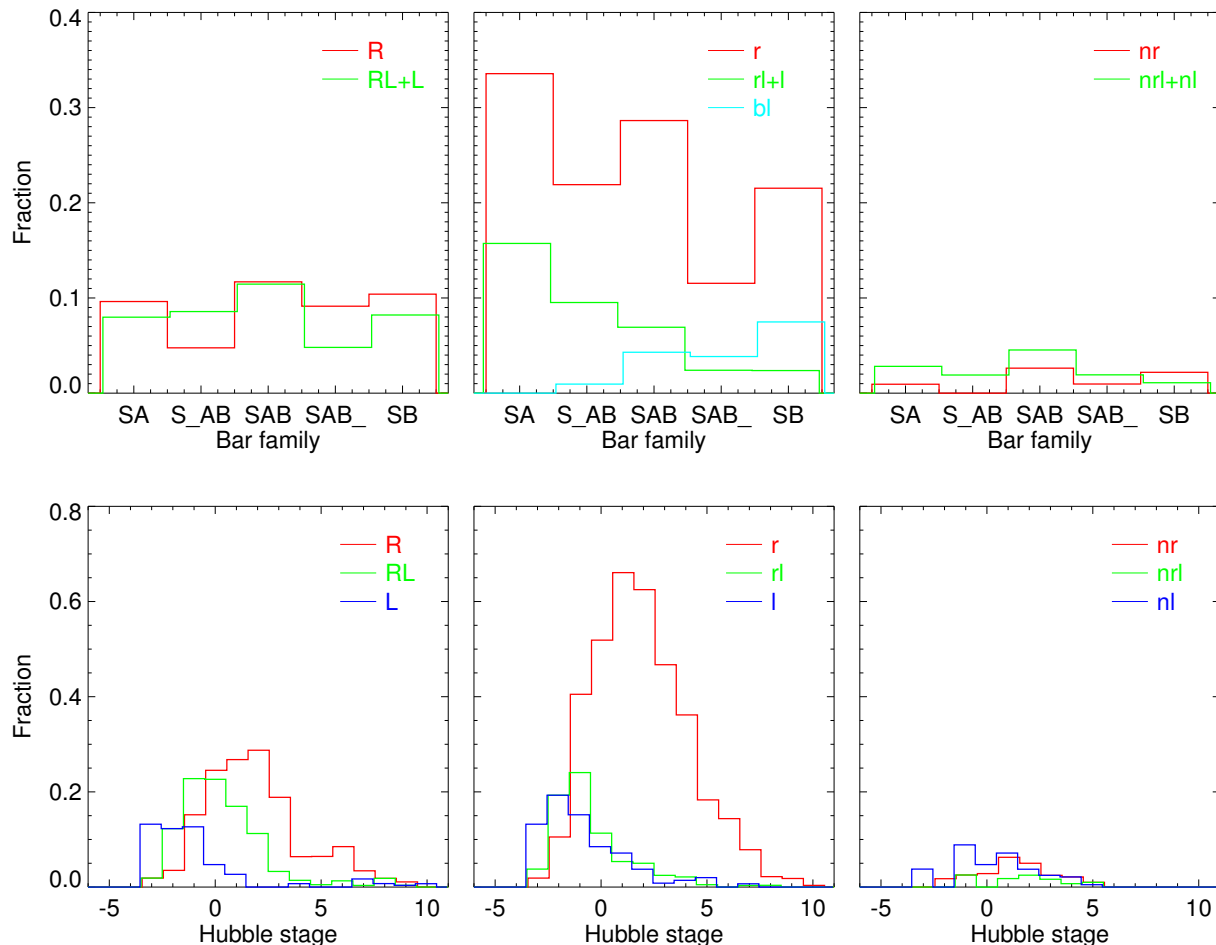
Fig. 9. Fractions of the measured features are shown as a function of the bar family (upper panel), and as a function of Hubble stage (lower panel). The normalization is made to all galaxies within each bar family class, and to the galaxies in the Hubble type bin. The half-integer Hubble types from Buta et al. (2015) were randomly rounded to the closest smaller or larger integer value. Again, the subcategories are included in the features.

sistent with the trend seen in Figure 10, if we assume that the decreased A mimics the increased halo contribution when moving to smaller mass galaxies. However, for the same range of simulated A's the nuclear ring increased even about 40%, and the outer ring shrank by 5%; there are no signs of these trends in Figure 10. Therefore, it is likely that several factors, like the ellipticity of the bar, pattern speed, or gas content might all affect the trend in the inner ring size.

For example, a straightforward interpretation of larger normalized inner ring size would be to assume that the bars of low mass systems are slower (larger R_{CR}/R_{bar}) than those in high mass systems. In this case, if we assume that the inner ring always resides at the UHR, the increase by a factor of about two in the normalized inner ring size when galaxy stellar mass M^* decreases from 10^{11} M$_\odot$ to 10^9 M$_\odot$ would imply a similar factor of two increase in R_{CR}/R_{bar} (neglecting any changes in the shape of rotation curve). A similar increase in the normalized size of outer rings would also be expected.

For barlenses the relative size seems to be independent of the parent galaxy mass (see Fig. 10a; the fit indicated by the dashed line is not statistically significant). Indeed, there is a close linear correlation between the size of a barlens and the size of a bar (see Fig. 11). This is a manifestation of the fact that barlenses indeed form part of the bar, which is consistent with the idea that bar-

lenses might indeed be the vertically thick inner parts of bars. For the appearance of barlenses the cut-off in the parent galaxy mass is similar to that of the nuclear features. This is not unexpected taking into account that barlenses appear in bright galaxies (see also Laurikainen et al. 2013), which also have bright central flux concentrations.

5.3.2. Sizes normalized to disk scalelength: comparison of barred and non-barred galaxies

In order to compare the sizes of the structure components between barred and non-barred galaxies, the sizes need to be normalized with a size measure independent of the bar. We have chosen to use the scalelength of the disk (h$_r$) given by P4 decompositions (Salo et al. 2015). The sizes of the various features as a function of the parent galaxy stellar mass are shown in Figure 12, in three bins of the family classes of bars. In Buta et al. (2015) the range $T_{bar} \geq 0.75$ corresponds to SB, the range $0.25 \leq T_{bar} < 0.75$ to SAB, and $T_{bar} < 0.25$ is for the non-barred galaxies. It appears that for the strong bars the inner, outer, and nuclear features occupy distinct regions, as they do in Figure 10a where they were normalized to the size of the bar. Barlenses also
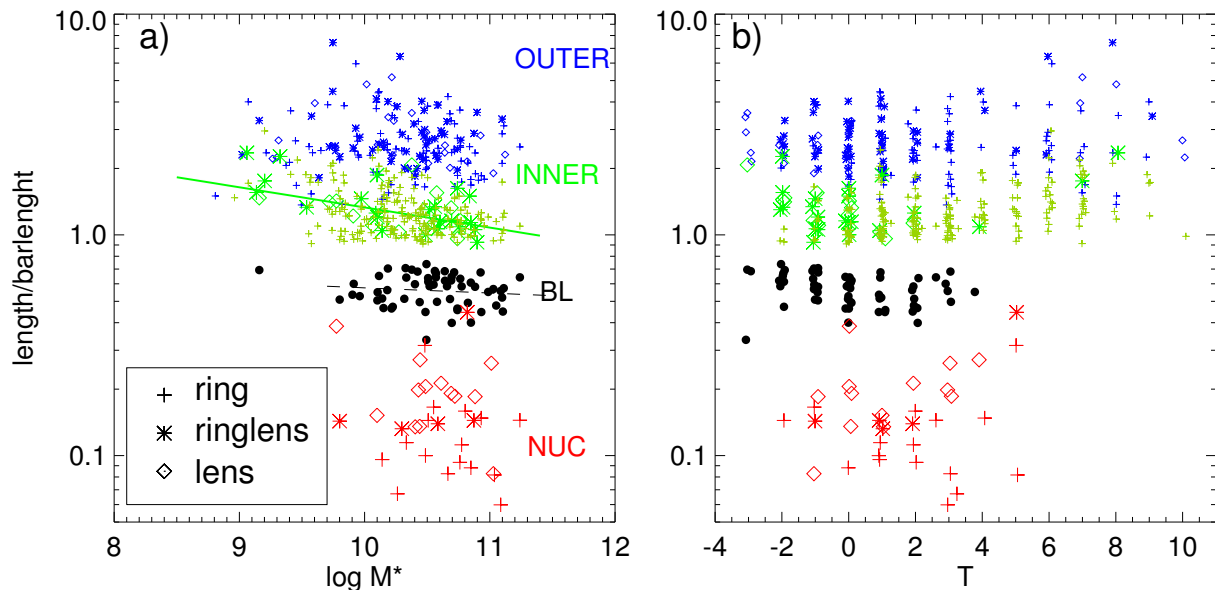
Fig. 10. The sizes of the measured features in barred galaxies shown as a function of (a) the parent galaxy mass and (b) the Hubble stage T. The sizes are normalized to the length of the bar. Shown with different colours are the inner (green), outer (blue), and nuclear (red) features, as well as barlenses (black). Within these feature categories rings, ringlenses, and lenses are shown with different symbols. Stellar masses are from P3 (Munoz-Mateos et al. 2015). The fit for inner structures (solid green line) is statistically significant, while the one for barlenses (dashed black line) is not.

occupy a similar region to that in Figure 10a. However, as can be expected the dispersion is now larger.

An interesting point in Figure 12 is that barlenses disappear while going towards weaker bars: they seem to be gradually replaced with rings, ringlenses, and lenses. This is very clear while looking at the non-barred galaxies: there is a distinct region of inner ringlenses and lenses, covering the same area as barlenses in the case of strongly barred galaxies. It is worth noticing that for barred galaxies this region is almost void of rings and lenses. Indeed, a considerable fraction of the inner lenses in the non-barred galaxies might be former barlenses in galaxies where the thin part of the bar has been dissolved. This conclusion was also made by Laurikainen et al. (2013) for the early-type disk galaxies in NIRS0S, based on the size histograms of the structures. However, compared to NIRS0S, in S^{4}G barlenses appear in a larger range of Hubble types and parent galaxy masses, and the dataset is also larger. Among the non-barred galaxies the region occupied by the inner features in the length/h$_R$ vs. M* diagram is quite broad, probably being a manifestation that not all inner features were formed by this mechanism.

For comparison, the outer and nuclear features in Figure 12 occupy quite similar regions in barred and non-barred galaxies. This suggests that matter is rearranged only close to the radius of the bar, where the orbital families behind the various structures are more easily mixed. If the barred potential changes during the evolution of the galaxy it should also affect the resonances of the bar. However, this does not necessarily affect the already created nuclear and outer features, if those structures, once formed, are dynamically decoupled from the barred potential. From Figure 12c it is also clear that not all inner lenses in the non-barred galaxies can be partly dissolved bars (those with sizes much larger than barlenses in barred galaxies). In fact, there might be two populations of lenses. The large lenses in the mass range of $M = 10^{10} - 10^{11} M_\odot$ could be triggered for example by minor mergers as suggested by Eliche-Moral et al. (2012).
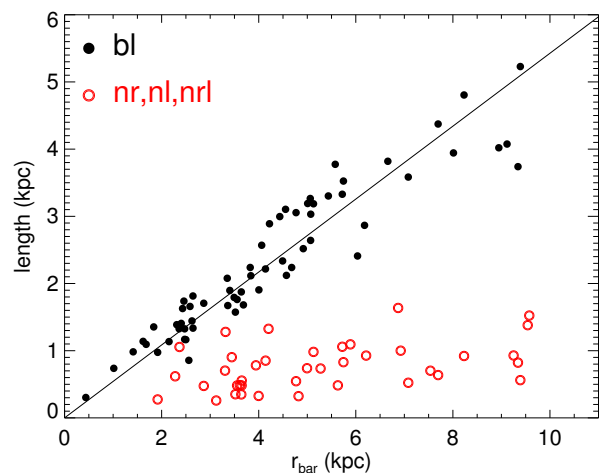

Fig. 11. The measured sizes of barlenses plotted as a function of the measured barlength, both given in kiloparsecs. The line shows a linear fit between these two parameters (slope = 0.54 forcing y-intercept = 0). For comparison, the measured sizes of the nuclear features are also shown, with no correlation with the barlength. However, it is important to note that the small nuclear structures may fall below the resolution of S^{4}G images (FWHM=2.1").

6. Summary and conclusions

A catalogue of the morphological features for the complete Spitzer Survey of Stellar Structure in Galaxies (S^{4}G), consisting of 2352 nearby galaxies, is presented. Using the 3.6 μm IRAC images, we have measured the dimensions and orientations of 1146 bars, 294 ringlenses and lenses, 87 nuclear features, and 67 barlenses. The pitch angles of the spiral arms were also measured, excluding the messy galaxies at the end of the Hubble
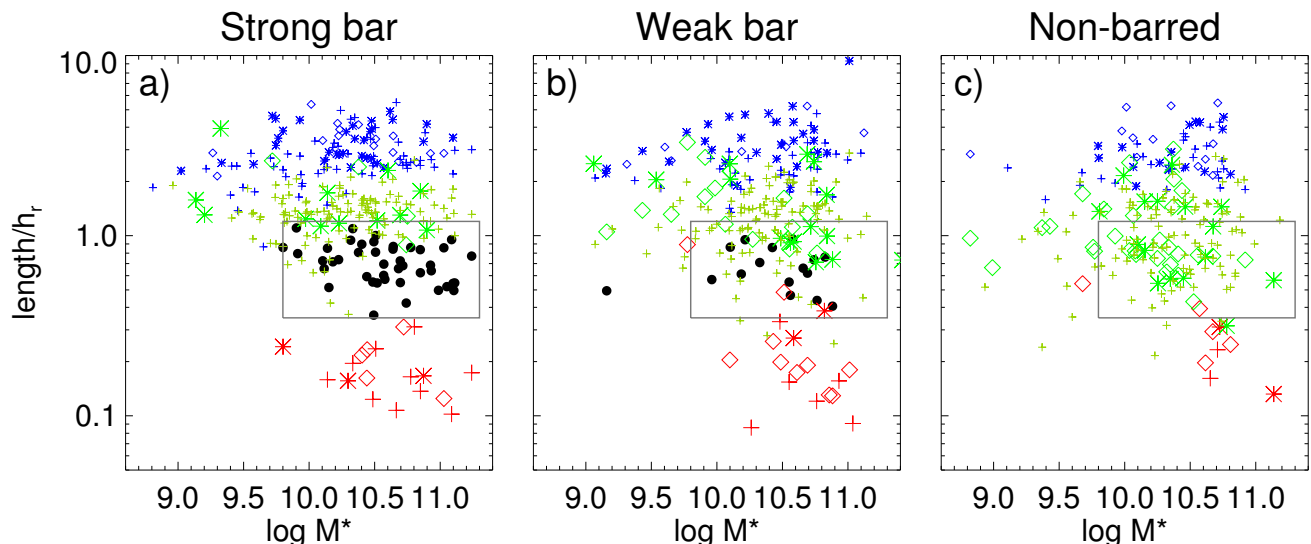
Fig. 12. A similar plot to that in Figure 11 (with the same symbols), but now the normalization is to the scalelength of the disk, h_r, taken from P4 (Salo et al. 2015). The three panels show the S^{4}G galaxies in different bins of the bar family so that bar strength decreases from (a) to (c). The box in all panels shows the region that covers the barlenses in the barred galaxies.

sequence. Multiple pitch angles for a single galaxy can appear. The measured parameters are given in Tables 2 and 3, the complete tables being available in electronic form. The catalogue is given as a web page[4]. Here we summarize our main conclusions:

(1) We confirm the previous results showing that inner and outer rings are peaked to later Hubble types (T=1) than lenses and ringlenses (T=-2). However, all types of structures appear in a wide range of Hubble types.

(2) The inner rings and lenses are found to appear preferentially in weakly barred (AB) and non-barred (A) galaxies. However, the appearance of outer and nuclear features does not depend on the family class of the bar (see Fig. 9).

(3) The sizes of the inner features correlate with the parent galaxy stellar mass, i.e. their sizes relative to the bar size are larger in the less massive galaxies (see Fig. 10).

(4) The size of a barlens has a tight linear correlation with the size of the bar (see Fig. 11), which provides additional support for the conjecture that barlenses indeed form part of the bar.

(5) Nuclear features and barlenses in barred galaxies appear only in galaxies more massive than $\sim 10^{10} M_\odot$, for barlenses because they appear only in strong bars that appear in bright galaxies. On the other hand, the nuclear features are lacking in the low mass galaxies because they lack ILRs due to low central mass concentrations.

(6) New observational evidence is shown indicating that a large fraction of lenses in the non-barred galaxies might be former barlenses of bars. The outer thin part of the bar might have dissolved or destructed, or might be too weak to be detected. This is manifested in the length/h_r vs. galaxy mass relation in such a manner that barlenses in strong bars (B) gradually turn into inner rings/lenses towards the non-barred galaxies (A)(see Figure 12).

References

Athanassoula, E. 1983, in IAU Symposium, Vol. 100, Internal Kinematics and Dynamics of Galaxies, ed. E. Athanassoula, 243–250
Athanassoula, E. 2005, MNRAS, 358, 1477
Athanassoula, E., Bosma, A., Creze, M., & Schwarz, M. P. 1982, A&A, 107, 101
Athanassoula, E., Laurikainen, E., Salo, H., & Bosma, A. 2014, ArXiv e-prints [arXiv:1405.6726]
Athanassoula, E., Romero-Gómez, M., Bosma, A., & Masdemont, J. J. 2010, MNRAS, 407, 1433
Boeker, T., Schinnerer, E., Lisenfeld, U., & Emsellem, E. 2004, in Bulletin of the American Astronomical Society, Vol. 36, American Astronomical Society Meeting Abstracts #204, 721
Bosma, A. 1983, in IAU Symposium, Vol. 100, Internal Kinematics and Dynamics of Galaxies, ed. E. Athanassoula, 253
Bournaud, F., Elmegreen, B. G., & Elmegreen, D. M. 2007, ApJ, 670, 237
Bureau, M., Aronica, G., Athanassoula, E., et al. 2006, MNRAS, 370, 753
Buta, R. 1986, ApJS, 61, 609
Buta, R. 1995, ApJS, 96, 39
Buta, R. & Combes, F. 1996, Fund. Cosmic Phys., 17, 95
Buta, R., Purcell, G. B., Cobb, M. L., et al. 1999, AJ, 117, 778
Buta, R., Sheth, K., Athanassoula, E., et al. 2015, ArXiv e-prints [arXiv:1501.00454]
Carollo, C. M., Stiavelli, M., Seigar, M., de Zeeuw, P. T., & Dejonghe, H. 2002, AJ, 123, 159
Combes, F. & Gerin, M. 1985, A&A, 150, 327
Combes, F. & Sanders, R. H. 1981, A&A, 96, 164
Comerón, S., Salo, H., Laurikainen, E., et al. 2014, A&A, 562, A121
Contopoulos, G. 1980, A&A, 81, 198
Davis, B. L., Berrier, J. C., Shields, D. W., et al. 2012, ApJS, 199, 33
Davis, B. L., Kennefick, D., Kennefick, J., et al. 2015, ApJ, 802, L13
Dekel, A., Sari, R., & Ceverino, D. 2009, ApJ, 703, 785
Díaz-García, S., Salo, H., Laurikainen, E., & Herrera-Endoqui, M. 2015, ArXiv e-prints [arXiv:1509.06743]
Draine, B. T. & Lee, H. M. 1984, ApJ, 285, 89
Eliche-Moral, M. C., González-García, A. C., Aguerri, J. A. L., et al. 2012, A&A, 547, A48
Elmegreen, B. G. & Elmegreen, D. M. 1985, ApJ, 288, 438
Elmegreen, B. G. & Elmegreen, D. M. 1989, ApJ, 342, 677
Elmegreen, B. G., Elmegreen, D. M., & Montenegro, L. 1992, ApJS, 79, 37
Elmegreen, D. M., Elmegreen, B. G., Yau, A., et al. 2011, ApJ, 737, 32

[4] http://www.oulu.fi/astronomy/S4G_STRUCTURES/main.html

Emsellem, E., Renaud, F., Bournaud, F., et al. 2015, MNRAS, 446, 2468
Erwin, P. 2005, MNRAS, 364, 283
Eskridge, P. B., Frogel, J. A., Pogge, R. W., et al. 2000, AJ, 119, 536
Fazio, G. G., Hora, J. L., Allen, L. E., et al. 2004, ApJS, 154, 10
Grouchy, R. D., Buta, R. J., Salo, H., & Laurikainen, E. 2010, AJ, 139, 2465
Jarvis, B. J. 1986, AJ, 91, 65
Kormendy, J. 1979, ApJ, 227, 714
Kormendy, J. & Kennicutt, Jr., R. C. 2004, ARA&A, 42, 603
Kormendy, J. & Norman, C. A. 1979, ApJ, 233, 539
Laurikainen, E. & Salo, H. 2015, in "Observed properties of boxy/peanut/barlens
    bulges" to appear in the book Galactic Bulges, ed. E. Laurikainen, R. F.
    Peletier, & D. A. Gadotti (Springer)
Laurikainen, E., Salo, H., Athanassoula, E., et al. 2013, MNRAS, 430, 3489
Laurikainen, E., Salo, H., Athanassoula, E., Bosma, A., & Herrera-Endoqui, M.
    2014, MNRAS, 444, L80
Laurikainen, E., Salo, H., Buta, R., & Knapen, J. H. 2009, ApJ, 692, L34
Laurikainen, E., Salo, H., Buta, R., & Knapen, J. H. 2011, MNRAS, 418, 1452
Lütticke, R., Dettmar, R.-J., & Pohlen, M. 2000, A&AS, 145, 405
Meidt, S. E., Schinnerer, E., Knapen, J. H., et al. 2012, ApJ, 744, 17
Muñoz-Mateos, J. C., Sheth, K., Gil de Paz, A., et al. 2013, ApJ, 771, 59
Muñoz-Mateos, J. C., Sheth, K., Regan, M., et al. 2015, ArXiv e-prints
    [arXiv:1505.03534]
Pfenniger, D. & Friedli, D. 1991, A&A, 252, 75
Salo, H., Laurikainen, E., Buta, R., & Knapen, J. H. 2010, ApJ, 715, L56
Salo, H., Laurikainen, E., Laine, J., et al. 2015, accepted to ApJS
Salo, H., Rautiainen, P., Buta, R., et al. 1999, AJ, 117, 792
Sandage, A. 1961, The Hubble atlas of galaxies
Sandage, A. & Bedke, J. 1994, The Carnegie Atlas of Galaxies. Volumes I, II.
Saraiva Schroeder, M. F., Pastoriza, M. G., Kepler, S. O., & Puerari, I. 1994,
    A&AS, 108, 41
Schwarz, M. P. 1981, ApJ, 247, 77
Schwarz, M. P. 1984, MNRAS, 209, 93
Seigar, M. S., Block, D. L., Puerari, I., Chorney, N. E., & James, P. A. 2005,
    MNRAS, 359, 1065
Seigar, M. S., Bullock, J. S., Barth, A. J., & Ho, L. C. 2006, ApJ, 645, 1012
Seigar, M. S., Chorney, N. E., & James, P. A. 2003, MNRAS, 342, 1
Seigar, M. S., Davis, B. L., Berrier, J., & Kennefick, D. 2014, ApJ, 795, 90
Sellwood, J. A. & Wilkinson, A. 1993, Reports on Progress in Physics, 56, 173
Sheth, K., Armus, L., Athanassoula, E., et al. 2013, Not Dead Yet! Completing
    Spitzer's Legacy with Early Type Galaxies, Spitzer Proposal
Sheth, K., Regan, M., Hinz, J. L., et al. 2010, PASP, 122, 1397
Sheth, K., Regan, M., Hinz, J. L., et al. 2014, in American Astronomical So-
    ciety Meeting Abstracts, Vol. 223, American Astronomical Society Meeting
    Abstracts 223, 205.02
Simmons, B. D., Melvin, T., Lintott, C., et al. 2014, MNRAS, 445, 3466
White, S. D. M. & Rees, M. J. 1978, MNRAS, 183, 341
Wozniak, H. & Pierce, M. J. 1991, A&AS, 88, 325
Yoshino, A. & Yamauchi, C. 2015, MNRAS, 446, 3749